Zhaoyun Ma
Department of Mechanical Engineering,
University of South Carolina,
Columbia, SC 29208
e-mail: zhaoyun@email.sc.edu

Lingyu Yu[1]
Department of Mechanical Engineering,
University of South Carolina,
Columbia, SC 29208
e-mail: yu3@cec.sc.edu

Yuh J. Chao
Department of Mechanical Engineering,
University of South Carolina,
Columbia, SC 29208
e-mail: chao@sc.edu

Poh-Sang Lam
Savannah River National Laboratory,
Aiken, SC 29808
e-mail: ps.lam@srnl.doe.gov

Robert L. Sindelar
Savannah River National Laboratory,
Aiken, SC 29808
e-mail: robert.sindelar@srnl.doe.gov

Andrew J. Duncan
Savannah River National Laboratory,
Aiken, SC 29808
e-mail: andrew.duncan@srnl.doe.gov

Thanh-Tam Truong
Savannah River National Laboratory,
Aiken, SC 29808
e-mail: thanh-tam.truong@srnl.doe.gov

Christopher Verst
Savannah River National Laboratory,
Aiken, SC 29808
e-mail: christopher.verst@srnl.doe.gov

Pei-Kang Sun
Department of Mechanical Engineering,
University of South Carolina,
Columbia, SC 29208
e-mail: peikang@mailbox.sc.edu

Andrew Campbell
Department of Mechanical Engineering,
University of South Carolina,
Columbia, SC 29208
e-mail: andrewpc@email.sc.edu

Nondestructive Evaluation of Stress Corrosion Cracking in a Welded Steel Plate Using Guided Ultrasonic Waves

Stress corrosion cracking (SCC) had occurred in early-generation high-level nuclear waste tanks constructed by welding carbon steel. This paper describes an ultrasonic inspection system and its fundamental ability to detect and quantify the length of SCC on thick welded steel plates. The finite element method (FEM) was applied to simulate the welding process to estimate the welding residual stress field. Growth of stress corrosion cracks is driven by crack stress intensities exceeding the subcritical cracking threshold intensity. The subject plate was experimentally inspected with ultrasonic nondestructive evaluation (NDE) techniques to characterize the extent of SCC. The NDE system uses a piezoelectric transducer to generate guided waves in the thick steel plate, and a scanning laser Doppler vibrometer (SLDV) to measure multidimensional time–space wavefield data over a user-defined scanning area in the plate surface. The measured wavefield data can show wave interactions in a localized area in the plate due to the presence of the discontinuities of the SCC. To generate an inspection image that can precisely show the crack's location and/or the dimension, the wavefield data are further processed to generate inspection image that maps the entire sample plate so the crack can be clearly identified in the plate while its length can be readily estimated. The ultrasonic test results for crack length agree well with the visually estimated length and are close to that predicted by the FEM for cracks in the weld residual stress field. [DOI: 10.1115/1.4053653]

Keywords: stress corrosion crack, finite element analysis, guided wave NDE, wavefield imaging, crack quantification, nuclear, testing methodologies, ultrasonics

1 Introduction

Large (0.75–1.3 million gallon capacity) steel tanks have been used for radioactive waste storage since the early 1950s at the Savannah River Site of the U.S. Department of Energy. Early generation designs of these storage tanks (types I and II) were manufactured by joining A285 carbon steel plates using a shielded metal arc welding or a submerged arc welding process [1,2]. During the

[1]Corresponding author.
Manuscript received July 21, 2021; final manuscript received January 7, 2022; published online March 1, 2022. Assoc. Editor: Paul Fromme.

welding process, residual stress could be introduced if the welded plates were not stress relieved with post-weld heat treatment. Subsequently, stress corrosion cracking (SCC) has been shown to occur under certain aggressive waste chemical conditions [1,2]. As a result, the radioactive materials can leak through the cracks to cause if the cracks penetrate the tank wall. Early detection of SCC is, therefore, crucial for timely response to provide mitigation and avoid extensive environmental insult.

Stress corrosion cracking has been inspected and monitored with various nondestructive evaluation (NDE) methods such as ultrasonic (longitudinal and/or shear wave), acoustic emission, Rayleigh waves, and electrochemical impedance spectroscopy methods [3–8]. Guided ultrasonic waves (GUW)-based NDE methods are relatively new. Guided waves are ultrasonic waves that propagate within the structural boundaries such as pipes and plates, and they can propagate long distance thus enabling large structure inspection [9,10]. The wave-damage interactions are used as indicators for structural discontinuity (i.e., damage) diagnosis. They were extensively studied and adopted in the past decades and have shown to be effective for crack detection and evaluation in metallic structures [11–19]. Exemplary works include instantaneous reference-free crack detection in thin metal structure [11], crack evaluation in thin aluminum plates using a 2D piezoelectric wafer made of zirconate titanate ceramics (PZT) array guided wave system [12], and the quantification of circumferential crack-like damage in pipelines through synthetically focused guided waves [13]. To give more examples, Lu et al. [20] used a network of PZT transducers in a 10-mm thick steel plate for fatigue crack evaluation. The crack can be located and the length can be roughly estimated using the wave energy derived from the wavelet transform of the time-domain signals. Qin et al. [21] traced the shifting of second harmonics in ultrasonic waves to detect surface cracks in a 3-mm thick aluminum beam. In addition to wave propagation methods, other methods such as nonlinear ultrasonics-based methods have also been studied to detect and quantify fatigue crack in thin aluminum plates. Wang et al. [22,23] used nonlinear ultrasonics with time reversal technique and demonstrated the detection of a fatigue crack in thin aluminum plates and the correlation between the damage indicators and crack growth. Of particular interest is the imaging method, where an image of the structure being inspected is generated with the area containing defects being highlighted. Such an image gives the detection as well as the estimation of the crack immediately. For example, Chen et al. [14] used the load-differential imaging method for fatigue crack detection and localization. Masserey and Fromme [16] studied the scattering of high frequency guided waves by a fatigue crack near a fastener hole on an aluminum plate, and Yu et al. [19] demonstrated crack detection and quantification in an aluminum plate using guided waves. Zima and Kędra [24] established an algorithm for line crack length estimation in a 1-mm thick steel plate by defining reflection coefficients and then using coefficients to create a damage map of the plate. The method was shown to be effective in detecting and locating a through-thickness cut crack but not in pinpointing the locations of the crack tips. Recent years with the use of scanning laser Doppler vibrometer (SLDV), wavefield measurements with respect to both time and space have become available, which provide abundant information about wave propagation characteristics to be used for imaging [15,19]. Wavefield measurements have been used for visualization and quantification of cracks [19,25–31]. Despite all the progresses, to the best knowledge of the authors, the ultrasonic guided wave inspection method has not been widely implemented for SCC detection and evaluation though some nonultrasonic methods have been reported in Ref. [32]. One example work of using ultrasonics is conducted by Hernandez-Valle et al. [17], where SCC was detected in stainless-steel pipes using a noncontact laser-laser/electromagnetic acoustic transducer ultrasonic system. However, the shape and dimension of the SCC were not obtained in the resulted wavefield image.

In this paper, we present the work on the detection and quantitative evaluation of SCC in a welded steel plate using the GUW-based NDE methods. The work began with the preparation of the welded test plate and exposure to simulated waste tank environments to initiate SCC, and conducting finite element analysis (FEA) to predict the generation and growth of SCC. The FEA simulated the exact welding process and used the relevant temperature history to calculate the residual stress distributions in the weldment and to evaluate the potential for stress corrosion cracking with a threshold stress intensity factor (K_{ISCC}) determined experimentally [33]. After FEA predicted the presence of the SCC, the plate was inspected using an ultrasonic guided wave scanning system. Multidimensional GUW wavefield was excited by PZT actuators, obtained by a SLDV, and then post-processed with imaging algorithms. With the resulted inspection images, not only the presence of the SCC could be confirmed as predicted by the FEA but also the crack length as well as its general shape is determined. While most previous work was focused on idealized electric discharge machining (EDM) cracks in thin metal plates, our work demonstrates the ability of GUW to detect and to estimate the length of barely visible SCC cracks in a thick stainless-steel plate with rugged surface. Despite the challenges from increased thickness and reduced crack size where guided waves propagation becomes complex and wave–crack interactions are weak to see, the filtering process can enhance the wave–crack interactions and line extract algorithm can provide a quick and effective estimation of the crack length. The remainder of the paper is organized as follows: Sec. 2 introduces the specimen preparation for initiating SCC and the FEA of welding simulation, residual stress calculation, and fracture mechanics evaluation. Section 3 describes GUW inspection setup as well as the imaging algorithms for SCC quantification, followed with Sec. 4 which applies the imaging method to detect two selected cracks by the PZT-SLDV system. The paper concludes with Sec. 5 summarizing the findings and the potential future work is also discussed.

2 Preparation of Plate Specimen and Stress Corrosion Cracking Growth

This section briefly describes the welding of the plate specimen and the fabrication of the starter cracks with EDM for SCC studies, and the FEA that was used to determine the welding residual stress by simulating the waste tank-specific welding procedure and to analyze crack growth. Stress intensity factors were calculated at the growing crack tip with FEA and compared with an experimentally determined threshold stress intensity factor [23], from which the maximum length of the stress corrosion crack could be predicted. This section aims to provide the background of the test specimen and the prediction of SCC so the NDE results can be compared.

2.1 Preparation of Stress Corrosion Cracking Specimen. The specimen is a welded steel plate (304.8 mm by 304.8 mm) manufactured by joining two 15.88-mm thick A285 carbon steel plates using gas metal arc welding (GMAW) with heat input in accordance with tank specifications [1,2], as illustrated in Fig. 1(*a*). The specimen was not heat treated to relieve the welding residual stress. After the welding, starter cracks (a total of nine) were fabricated with EDM across or along the weld in various locations and with different orientations as illustrated in Fig. 1(*b*). Among the nine starter cracks, only V1, V2, and V3 are through-thickness vertical cracks across the weld. The other starter cracks are part-through-thickness semicircular cracks with a depth of 6.35 mm. More details about the starter cracks can be found in Ref. [1].

The plate was then submerged in 5 molar (5M) sodium nitrate ($NaNO_3$) solution (prepared with reagent grade compound and distilled water) at about 90 °C for up to ten weeks to initiate and propagate SCC. In fact, SCC was visually observed after 2 weeks of exposure to the solution. By the end of the corrosion test, SCC was only observed from the through-thickness vertical starter cracks (V1, V2, and V3) with final crack lengths estimated ranging from 40 mm to 150 mm (including the starter crack across the weld of

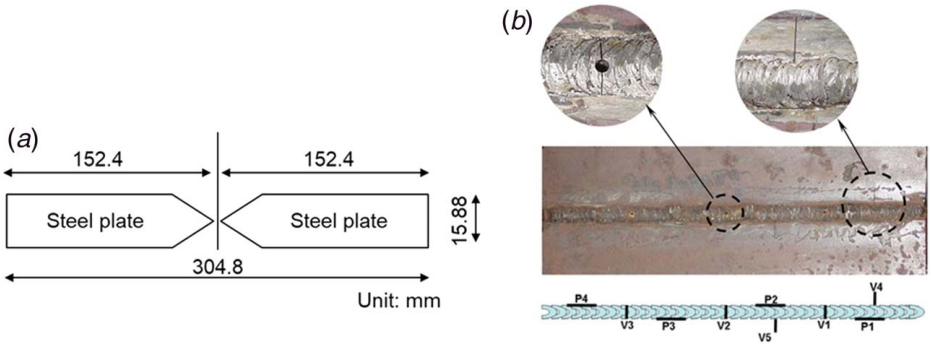

Fig. 1 Specimen preparation: (*a*) schematic of two steel plates before being joined by GMAW and (*b*) zoom in pictures of the welded area with EDM starter cracks after the GMAW joining [1]

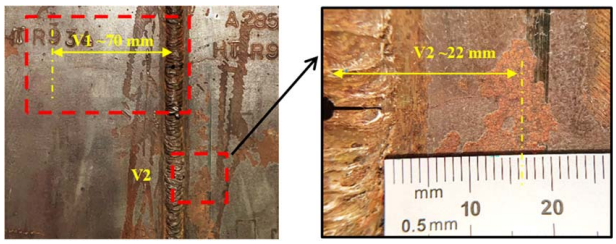

Fig. 2 Visual inspection of stress corrosion cracking V1 and V2 (image of V2 was obtained with the aid of a hand hold magnifier)

12.5 mm). From Fig. 2, it can be seen that V1 has the longest visible SCC growth (about 70 mm in the half of the welded plate), while V2 has the shortest SCC by visual inspection, which is barely visible with unaided eyes. The V2 crack length in the half welded plate was estimated at about 22 mm with a hand-held magnifier. Details of the specimen and SCC test can be found in Ref. [1].

2.2 Finite Element Analysis Modeling and Stress Corrosion Cracking Growth Study. A three-dimensional finite element analysis was performed to validate the presence of SCC before the NDE inspection is performed. Only half of the plate was needed for modeling because of symmetry. Figure 3(*a*) shows the finite element mesh for the intact plate without EDM starter cracks, which contains 6780 eight-node brick elements with 8723 nodes. The detailed mesh in the V-groove area of the weld is shown in Fig. 3(*b*), where the six welding passes are identified [1]. A heat transfer analysis was first conducted to simulate GMAW using WeldSim, a three-dimensional welding finite element program [34–36]. The temperature history from the GMAW simulation was generated and then fed to the ABAQUS finite element program [37] for calculating the as-welded residual stresses through thermomechanical computational procedure.

For the subsequent fracture analysis, the finite element mesh was refined in the starter crack locations (Fig. 4). The initial as-welded residual stress for the refined mesh was established by interpolating the previously obtained residual stress through an ABAQUS mesh-to-mesh solution mapping feature [37]. The starter cracks were then introduced to the model by creating new, traction-free surfaces (Figs. 4(*a*) and 4(*b*)). The unbalanced stresses in the new cracked model were to be equilibrated by invoking the boundary change procedure in ABAQUS. The resulting residual stress was used to calculate the stress intensity factors for these starter cracks. It was found [1] that only the stress intensity factors for the through-thickness starter cracks (V1, V2, and V3) were greater than the threshold stress intensity factor (K_{ISCC}), which was experimentally determined as 35 MPa $\sqrt{m}$ in Ref. [33]. This indicated that only V1, V2, and V3 were likely to initiate SCC in the as-welded residual stress field, and the other starter cracks shown in Fig. 1(*b*) would remain stationary.

The growth of SCC was simulated in a self-similar manner (i.e., the crack front remains straight and through the thickness), as schematically shown in Figs. 4(*a*) and 4(*b*). The process created a continuous redistribution of the residual stress as the crack is growing and allowed the stress intensity factors to be determined as a function of crack growth. By setting a threshold stress intensity factor K_{ISCC} to 35 MPa $\sqrt{m}$ [1], the maximum likely achievable crack length at V2 under welding residual stress was predicted to be 39 mm in half of the plate based on such a cracking criterion [1].

3 Laboratory Inspection Through Guided Ultrasonic Waves Nondestructive Evaluation

The FEA has predicted that V1, V2, and V3 would grow in the test specimen and a crack growth analysis was conducted for

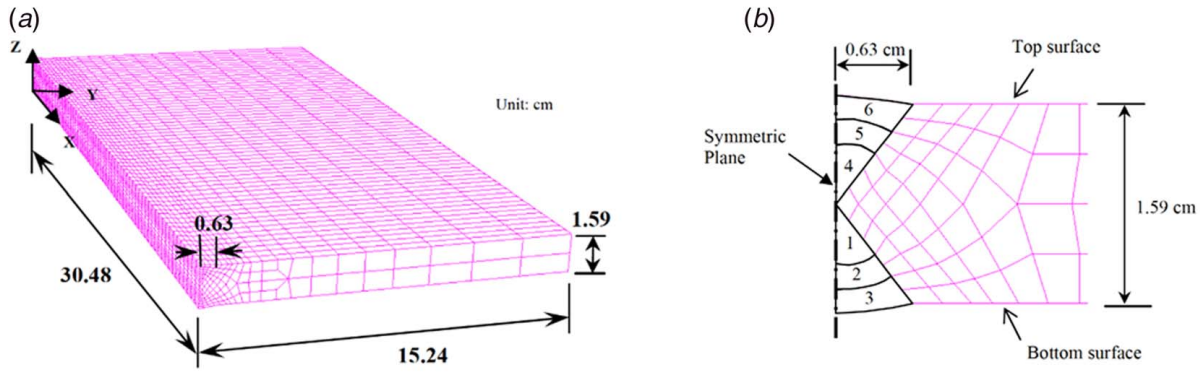

Fig. 3 (*a*) Three-dimensional finite element model for welding simulation and thermomechanical analysis and (*b*) detailed finite element mesh in the V-grooves showing the six passes of welding [1]

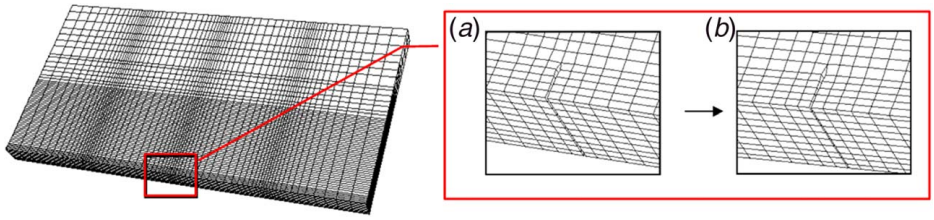

Fig. 4 Finite element mesh for modeling through-thickness crack growth from (*a*) a shorter crack to (*b*) a longer crack [1]

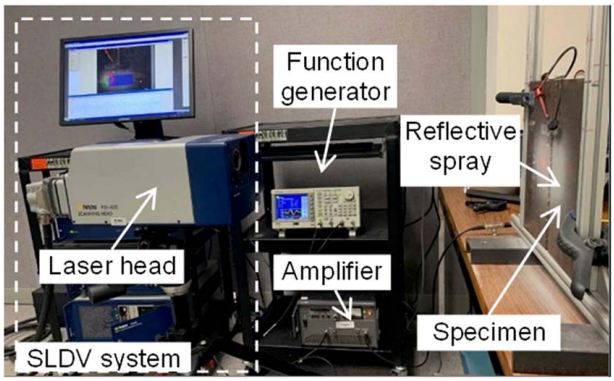

Fig. 5 Experimental setup of the PZT-SLDV inspection system [26]

V2 [1]. In this section, GUW NDE is adopted to experimentally inspect and evaluate the most significant V1 and the shortest but more challenging V2 in the test plate using a scanning GUW system and multidimensional wavefield imaging algorithms. When waves propagate in the plate and encounter structural discontinuities such as cracks, waves will be modified as being reflected, scattered, or transmitted through. By extracting the wave-discontinuity interaction features, the discontinuity can be detected and evaluated quantitatively.

3.1 The PZT-SLDV System for Stress Corrosion Cracking Inspection. A scanning GUW system that obtains time–space propagating guided waves has been previously developed [15]. The system uses a PZT wafer to actuate the waves through the piezoelectric effect [10] and a SLDV to measure the resulted wave propagation in the structure with respect to both time and space. The SLDV measures surface particle out-of-plane velocity (with respect to time) based on Doppler effect [15] point by point in a user-defined scanning grid. The obtained wavefield can directly show wave–damage interaction, which can facilitate the damage evaluation process [38–40].

The laboratory setup of the PZT-SLDV GUW system is illustrated in Fig. 5. A Tektronix AFG3022C function generator is used to generate the excitation signal. In this study, the excitation is a three-count toneburst at a desired excitation frequency. The excitation signal is amplified by a NF HSA 4014 bipolar amplifier and then sent to the PZT wafer actuator. The PZT (by STEMINC, with 7 mm diameter and 0.5 mm thickness) is bonded on the specimen surface using adhesive. Upon the application of the excitation to the PZT, waves are generated through in-plane piezoelectric coupling [10] and propagate in the plate governed by the Rayleigh–Lamb equation [25]. The waves are then measured by the SLDV (Polytec, Model No. PSV-400-M2) to generate time–space wavefield data. Note that the SLDV head is placed in a way that the laser beam impinges normal to the specimen surface, thus only surface particle velocity along the out-of-plane direction will be measured. Details of SLDV for guided waves sensing can be found in a previous study [41]. In order to improve the surface reflectivity for SLDV measurement, wipe-off reflective spray (by Albedo 100) is applied to achieve good signal quality.

In the NDE part of the study, the validation test for SCC detectability was first conducted for V1 crack which has the longest SCC, then V2 crack (shortest) was tested to explore the resolution of the subject GUW method. Only half of the cracks in the half plate were inspected (all crack lengths are half plate length throughout the subsequent discussion). With visual examination, the estimated length of V1 was about 70 mm and V2 about 22 mm. The actuation and sensing schematics for V1 and V2 are outlined in Figs. 6(*a*) and 6(*b*), respectively. For each crack, two inspections were performed with (1) a PZT actuator placed normal to the expected crack growth direction (denoted as PZT-1 and referred to as "normal" inspection) and (2) a PZT actuator in line with the length of the crack (denoted as PZT-2 and referred to as "parallel" inspection), respectively. The SLDV scanning area for V1 is about 100 mm by 50 mm and for V2 is about 35 mm by 20 mm, as indicated by the dotted rectangles in Fig. 6. Cartesian coordinates are defined with PZT-1 as the origin for V1 scan and the EDM starter hole as the origin for V2 scan.

3.2 Guided Waves Setup and Inspection. Excitation frequency tuning study [25] was first performed to identify a suitable inspection frequency that not only excited adequate amount of

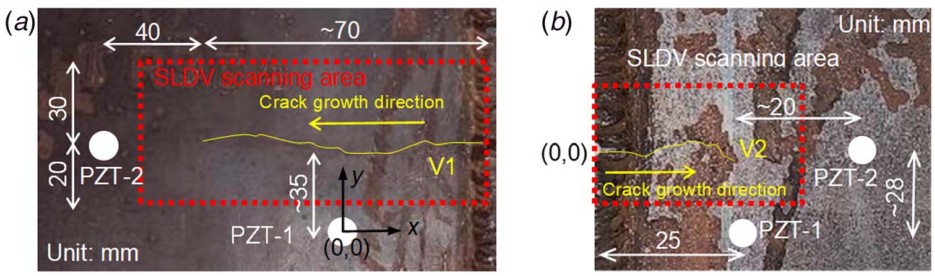

Fig. 6 Actuation and sensing scheme for the 2D inspection of (*a*) V1 [26] and (*b*) V2. Note that two actuation locations are investigated for each SCC with normal (PZT-1 for actuation) and parallel (PZT-2 for actuation) inspection, respectively.

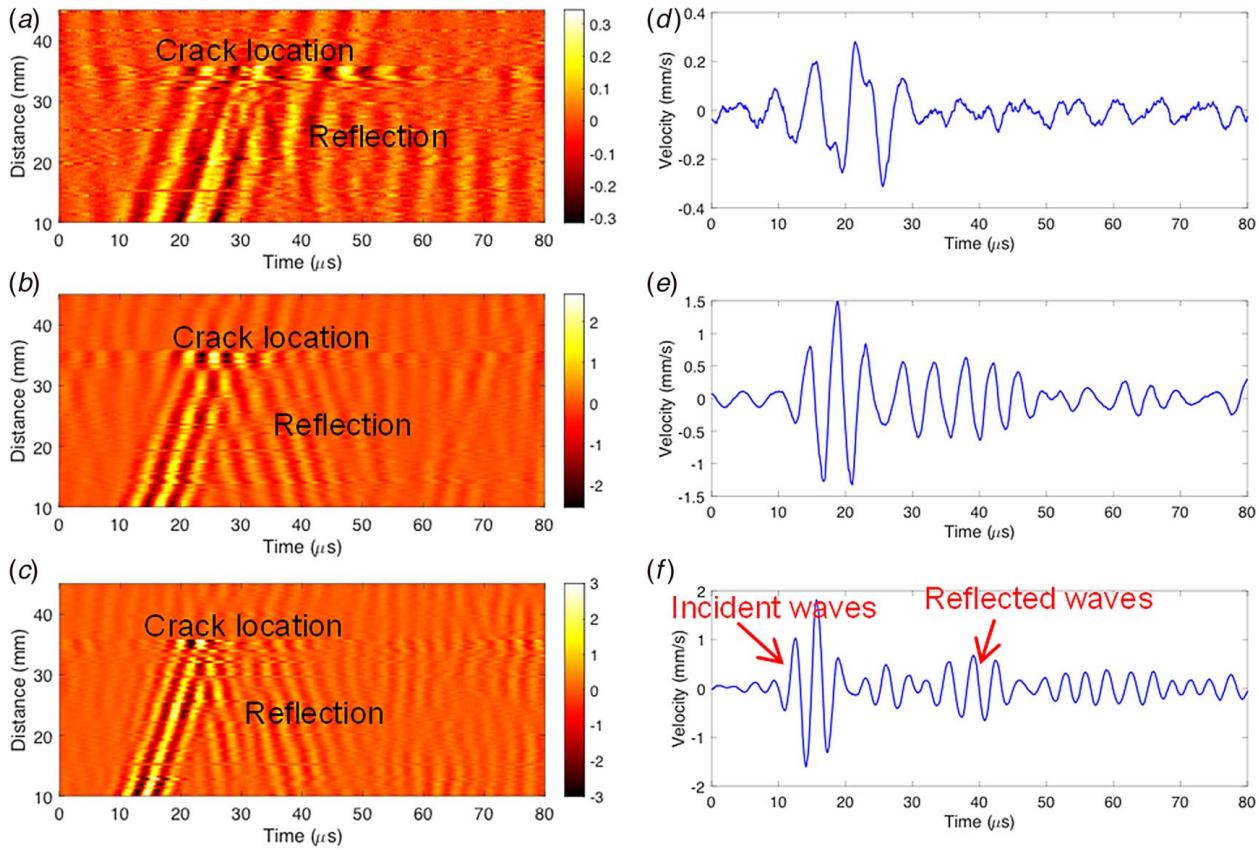

Fig. 7 Inspection frequency study: time–space wavefield obtained at (*a*) 120 kHz, (*b*) 210 kHz, and (c) 300 kHz; and waveform at 15 mm obtained at (*d*) 120 kHz, (e) 210 kHz, and (*f*) 300 kHz

guided waves to propagate in this plate but also interacted optimally with the crack to result in maximized reflections or scatterings in the waves. This study was conducted at V1 using PZT-1. Three inspection frequencies at 120, 210, and 300 kHz were shown and illustrated in Fig. 7. A toneburst with peak-to-peak amplitude 50 V was used for excitation. Three line SLDV scans along y-axis with a spatial resolution of 0.5 mm were performed. To improve the signal quality, 30 averages were performed for each of the SLDV measurement.

The measured time–space wavefields are plotted in Fig. 7, which shows the presence of wave–crack interactions as reflections and reduced transmission beyond the crack. However, the result of the 300 kHz excitation frequency (Fig. 7(*c*)) gave the most discernible identification of such phenomenon, particularly the reflections that served as an indicator for the presence of the crack. Note that the magnitude scales are different in each case. To further evaluate the results, the signal-to-noise ratio (SNR) was also examined for each case by extracting a single waveform. The waveforms obtained at $y = 15$ mm are shown in Fig. 7. The SNR is calculated as the maximum magnitude of the waveform divided by the floor noise. The waveform comparison confirmed that the 300 kHz case (Fig. 7(*f*)) presented the waves of the highest strength in the plate and yielded the best SNR. Moreover, the reflections from the crack were best observed for 300 kHz in Fig. 7(*f*), but was not distinguishable in other cases. Therefore, 300 kHz was chosen to be the inspection frequency for the subsequent SCC NDE in this work.

With the selection of excitation frequency of 300 kHz, the area scans for both V1 and V2 cracks using normal and parallel inspections were performed and the resulted wavefields are presented in Fig. 8. Figures 8(*a*) and 8(*b*) give the results from V1 inspection. For normal inspection, the excited guided waves interacted strongly with the V1 where reflected waves could be clearly observed. In addition, most of the waves were blocked by V1, thus waves barely transmitted beyond V1 as shown in Fig. 8(*a*). Different wave–crack interaction phenomena were observed, however, for the parallel inspection. Fig. 8(*b*) shows that the wave intensity (indicating wave energy) increased along the V1 crack line but no reflected waves were observed. The reason is that, due to this setup, the incoming waves interacted with the crack dimension in width and, while the waves propagated along the crack, some wave energy was trapped and "flowed" within V1. Further study will be pursued in the future to understand the details of the interaction mechanism. The wavefield results showed that wave interactions with the crack could be used as direct evidence of structural damage. The inspection results of V2 are presented in Figs. 8(*c*) and 8(*d*). Since V2 is much shorter than V1, the scanning area was accordingly reduced. From the normal inspection, the wave interactions with V2 were weak and indeed a challenge to identify its presence by examining the wavefield snapshots in Fig. 8(*c*). Similar observation for parallel inspection can be seen from Fig. 8(*d*). This is expected since V2 is short and the crack line is difficult to observe by visual inspection without the aid of a magnifier.

4 Guided Ultrasonic Waves Imaging for Stress Corrosion Cracking Detection and Evaluation

Using the SLDV time–space wavefield snapshots, the wave–crack interaction can be identified and is used as an indicator for the presence of a crack. It also provides an estimation of crack location. However, the exact dimension or shape of the crack remains to be determined. In this section, an imaging algorithm has been developed and applied to the acquired wavefield data to generate an intensity energy map where the crack is highlighted. A crack line is further extracted from that energy map to determine its length.

4.1 Guided Ultrasonic Waves Imaging Method. The time–space wavefield data recorded by the SLDV is denoted as $v(t,\mathbf{x})$

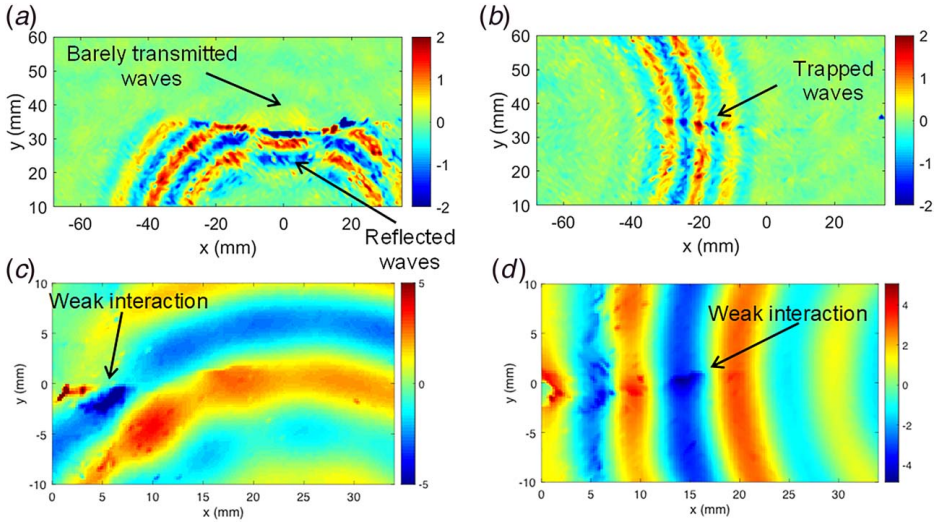

Fig. 8 Time–space wavefield snapshot at 20 μs showing the wave interactions with V1: (*a*) normal inspection and (*b*) parallel inspection [26]; and time–space wavefield snapshot at 25 μs showing the wave interactions with V2: (*c*) normal inspection and (*d*) parallel inspection

where t represents the time information recorded and $\mathbf{x}$ represents the spatial coordinates in the targeted scanning area. Note $\mathbf{x}$ can represent either 1D spatial information as x or 2D spatial information as (x,y) depending on the sensing schematic. In the literature, different imaging methods have been reported for the wavefield data processing to quantify damage [19,40,42,43]. In this study, a three-step frequency–wavenumber filtering [19] based imaging process was adopted for the wavefield data $v(t,\mathbf{x})$: (1) generating an wavefield energy map for quick inspection, (2) applying a frequency–wavenumber filter-based imaging method to generate the wavefield energy map induced by damage, and (3) extracting the crack line using the imaging results of step (2). The details of the method are given as follows.

First, a wavefield energy map $E(\mathbf{x})$ is generated by calculating the cumulative mass-normalized kinetic energy at each point (x,y) in the scanning area in the total recording time (t) [42]

$$E(\mathbf{x}) = \int_0^t \frac{1}{2}(v(\tau, \mathbf{x}))^2 \mathrm{d}\tau \tag{1}$$

However, with the directly generated energy map by Eq. (1), the damage location and general shape can often be indicated, yet not fully quantified [44]. Multidimensional Fourier analysis of the wavefield data has been widely adopted to convert the time–space information to the corresponding frequency–wavenumber domain, which contains a wealth of wave characteristics including the wave mode, frequency, and wavenumber information. Details of the Fourier analysis can be found in the literatures [45,46]. Only essential steps are given here for explaining the imaging method in the study. Hence, the second step of the imaging is to apply the Fourier transform to the wavefield data $v(t,\mathbf{x})$:

$$V(f, \mathbf{k}) = \int_{-\infty}^{\infty}\int_{-\infty}^{\infty} v(t, \mathbf{x}) e^{-j(2\pi ft + \mathbf{k}\cdot\mathbf{x})} \mathrm{d}t\mathrm{d}\mathbf{x} \tag{2}$$

where f is the frequency (the counterpart of time t) and $\mathbf{k}$ as (k_x, k_y) is the wavenumber vector (the counterpart of the spatial vector $\mathbf{x}$). In the f–k representation $V(f, \mathbf{k})$, new wavenumbers are expected to occur when damage occurs as compared with the pristine case. These new wavenumbers can then be extracted by applying a suitable frequency–wavenumber filter $F(f, \mathbf{k})$ by multiplying the original $V(f, \mathbf{k})$ with filter $F(f, \mathbf{k})$. The filtered wavefield $V_D(f, \mathbf{k})$ is thus obtained as

$$V_D(f, \mathbf{k}) = V(f, \mathbf{k})F(f, \mathbf{k}) \tag{3}$$

With $V_D(f, \mathbf{k})$, an inverse Fourier transform is applied to convert it back to the time–space domain, resulting in the damage-induced wavefield as

$$v_D(t, \mathbf{x}) = \frac{1}{(2\pi)^2}\int_{-\infty}^{\infty}\int_{-\infty}^{\infty} V_D(f, \mathbf{k}) e^{j(2\pi ft + \mathbf{kx})} \mathrm{d}f\mathrm{d}\mathbf{k} \tag{4}$$

By applying Eq. (1) to the filtered wavefield $v_D(t, \mathbf{x})$, an energy map $E_D(\mathbf{x})$ that corresponds only to the damage can be generated.

The final step is to extract the crack line from the energy map. This is achieved by finding the coordinates corresponding to the maximum energy intensity along the y direction in this study, which will give maxima at various x locations, as

$$y(x) = \arg\max_y |E_D(x, y)| \tag{5}$$

4.2 Crack Imaging and Estimation. The wavefield data given in Fig. 8 are now processed with the imaging algorithms outlined in Sec. 4.1. The energy map images of V1 using the wavefields obtained by PZT-1 for normal inspection and PZT-2 for parallel inspection are presented in Figs. 9(*a*) and 9(*b*), respectively. For the normal inspection (Fig. 9(*a*)), the waves gradually attenuate and decrease as they propagate away from the excitation source. When the waves arrive at and interact head-on with the entire crack, distinctive energy distribution change is observed in the area before the crack (extensive) and that after the crack (barely any), with a clear boundary in between. Such a distribution of energy is consistent with the wave phenomenon in the case, where the wavefront is normal to the long crack. In such a situation, most of the waves are blocked when they encounter V1 and reflected with barely any transmitting around it. The energy map image allows the estimation of V1 crack length, which is about 70 mm along the x direction by visually tracing the energy distribution boundary. It is close to the visual measurement of ~70 mm (Fig. 6(*a*)).

The energy map generated from parallel inspection wavefield is given in Fig. 9(*b*). In this case, the waves interact with the very small width of the SCC crack. Along the crack, a small amount of energy is trapped and highlighted in the map in Fig. 9(*b*), while the rest of waves continue the propagation and attenuation pattern. The crack length can also be estimated as about 69 mm along the x direction by visually tracing the line formed by the trapped energy. It is consistent with the estimation that was obtained from the normal inspection.

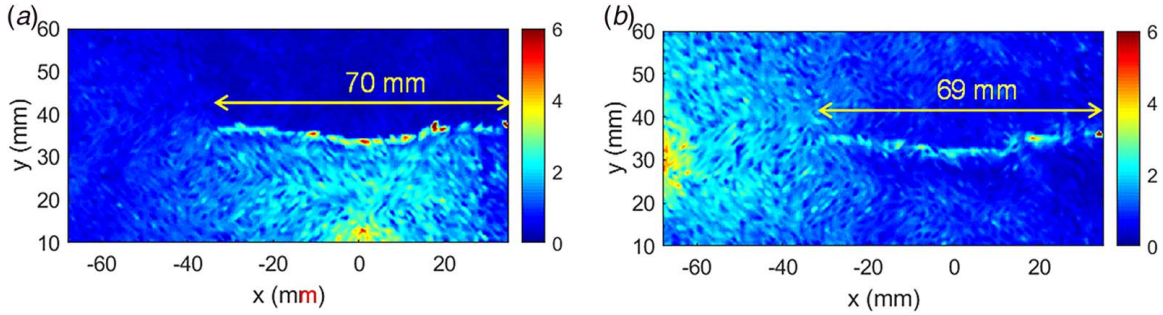

Fig. 9 Energy map of (*a*) normal inspection with PZT-1 as actuator and (*b*) parallel inspection with PZT-2 as actuator, with the V1 length and shape quantified [26]

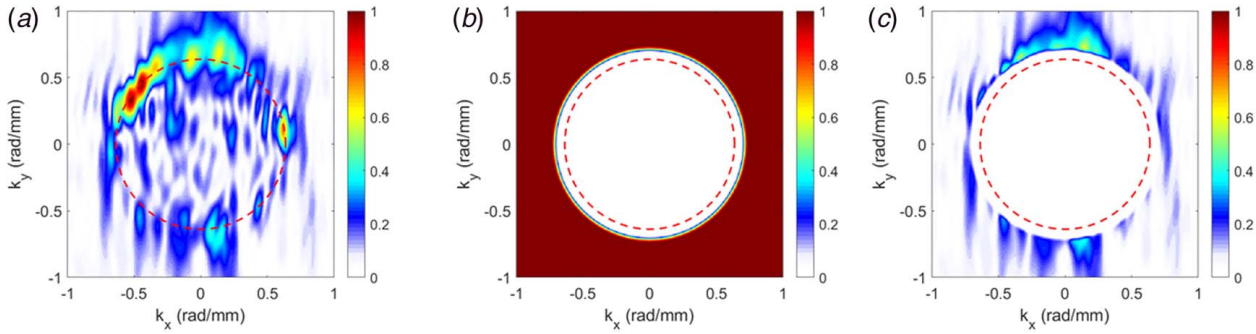

Fig. 10 Filtering process to extract the SCC-induced wavenumber components for normal inspection: (*a*) wavenumber spectrum at 300 kHz, (*b*) high-pass filter used to filter the crack-induced high wavenumbers at 300 kHz, and (*c*) filtered crack-induced high wavenumbers at 300 kHz

As seen in Fig. 9, the direct imaging results also include the energy of the incident waves from the excitation source toward the defect. The energy from the source or the incident waves is comparatively strong or even stronger than that induced by the damage, causing certain illusion in the detection. Hence, an image that includes only the defect induced/scattered energy will be more convenient for identifying and quantifying the defect. In this application, the filtering process, outlined in Sec. 4.1, is adopted to remove the source and incident energy in the energy map by applying a high-pass filter. The filtering process is illustrated here with the wavefield data from normal inspection. The wavefield data are first transformed to *f–k* domain using 2D Fourier transform given in Eq. (2). The obtained *f–k* spectrum at 300 kHz is presented in Fig. 10(*a*). Note the dash circle is the theoretical fundamental guided Lamb wave A_0 wavenumber curve at 300 kHz. The comparison with respect to the theoretical curve also confirms that the waves in the plate are dominated by the A_0 waves. It can be seen that there are wavenumbers other than those around the theoretical values appearing. Based on the previous studies [19,47], cracks usually induce higher wavenumbers corresponding to abruptly reduced structural dimension (thickness) for the plate, and thus the higher wavenumbers than the theoretical values are considered crack induced. To extract the higher wavenumbers, a high-pass filter as illustrated in Fig. 10(*b*) is applied to the original *f–k* spectrum (Fig. 10(*a*)) using Eq. (3). Figure 10(*c*) presents the filtered *f–k* spectrum with only higher wavenumbers induced by the crack being retained. Through inverse Fourier transform (Eq. (4)), the filtered *f–k* spectrum is transferred back to time–space domain, resulting a wavefield with only crack-induced waves due to scattering at such structural discontinuity. Finally, an energy image is obtained using the crack-induced waves' wavefield. Similar to the processing of normal inspection result, the filtering process of retaining higher

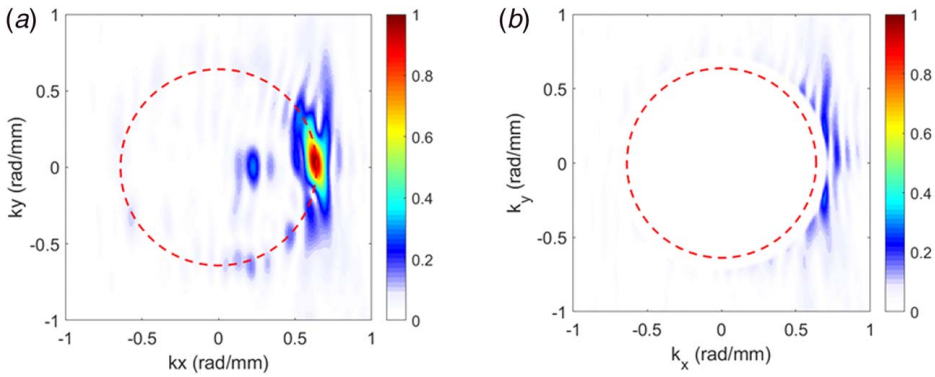

Fig. 11 Wavenumber spectrum at 300 kHz for parallel inspection: (*a*) original spectrum and (*b*) filtered crack-induced wavenumbers

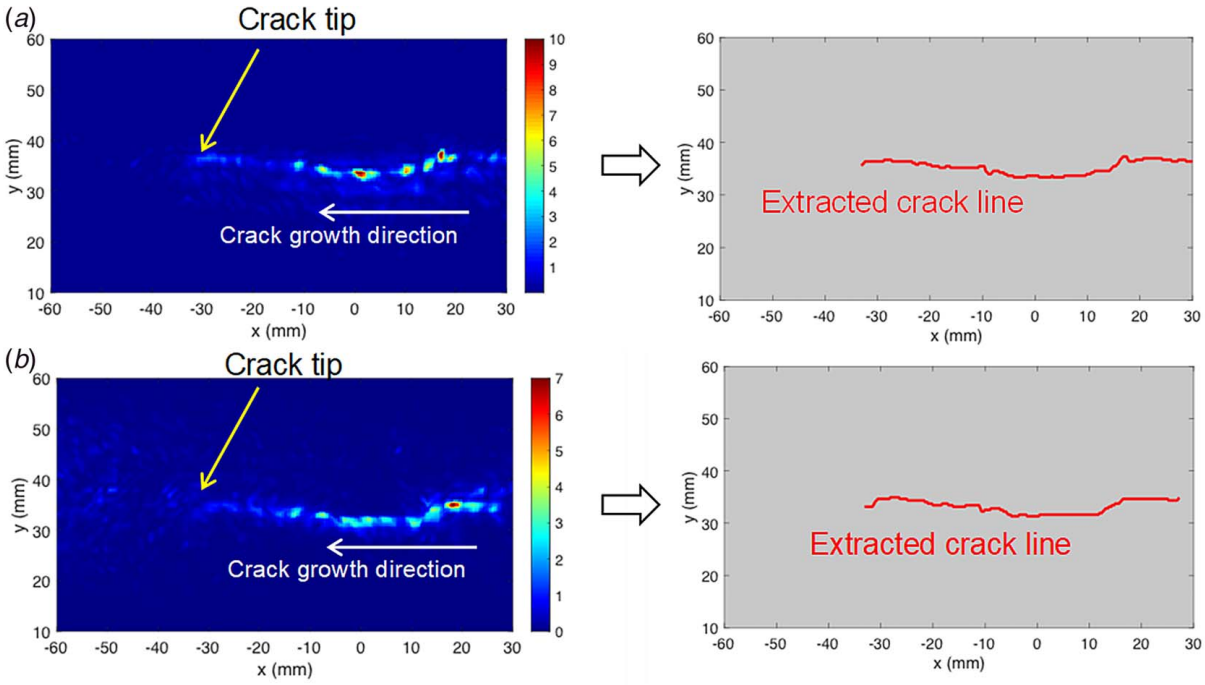

Fig. 12 V1 imaging and extracted crack line results: (*a*) normal inspection and (*b*) parallel inspection

wavenumbers is applied to the parallel inspection. The original wavenumber spectrum at 300 kHz and the filtered crack-induced high wavenumbers at 300 kHz are given in Fig. 11.

The resulting crack-induced energy images are shown in Fig. 12 on the left for both normal and parallel inspections. It can be seen that high intensity pixels are present along the actual V1 crack in both inspections, with weaker intensities at the crack tip. The estimation of crack size by visually tracing the highlighted areas in the energy map can be further enhanced by image post-processing to extract the crack line using Eq. (5). In the extraction post-processing, outliers are identified if the pixel's y location is more than 1 mm away from the previous point; and the outlier's y location will be corrected by using that of the previous point. In addition, interpolation is performed after the extraction process to smooth out the crack line. The extracted crack lines for V1 are plotted in Fig. 12 for both the normal and parallel inspections.

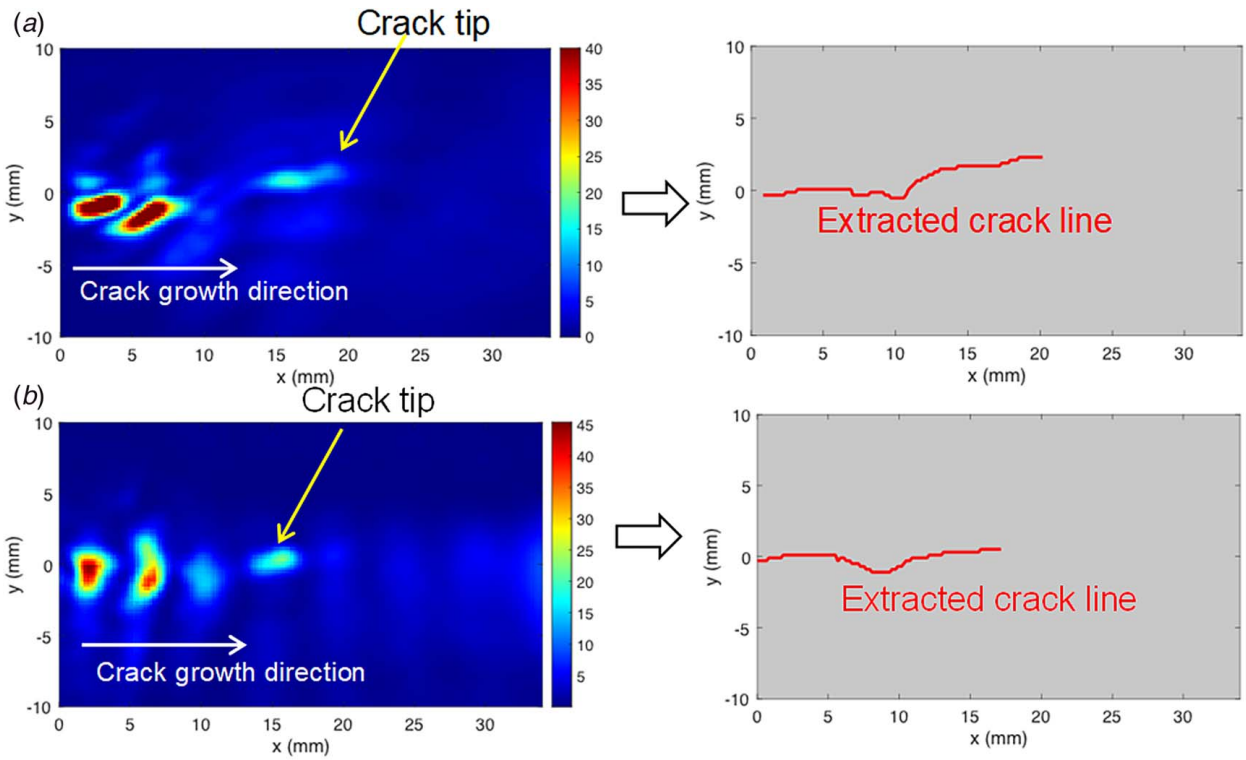

Fig. 13 V2 imaging and extracted crack line results: (*a*) normal inspection and (*b*) parallel inspection

Both inspections yield an estimation of about 65 mm for the V1 crack. By comparing with the energy images as well as the actual crack through visual inspection, it can be seen that the extracted crack line is also consistent with the general shape of the crack. The results show that the filtered imaging combined with the crack line extraction provides an effective and direct way to evaluate line SCC cracks.

With the success of adopting the detection and imaging on V1 crack, the methods are also applied to the more challenging shorter V2 crack in the plate. The results are given in Fig. 13. For both normal and parallel inspections, V2 crack can only be partially traced because of significantly weaker wave–crack interaction for this much smaller crack. The areas with the high pixel values correspond to the "root" of the V2 crack where it started growing from stress concentrated weld zone and the initial hole-cut. Moving rightward along the crack growth direction, V2 crack becomes much smaller and barely discernable by visual inspection, resulting the much weaker energy intensity toward the tip around 15–20 mm. Further being processed with the crack extraction method, however, we are able to derive an indication of V2 crack which is comparable to the shape observed from visual inspection. The extracted crack lines give an estimation of crack length of about 20 mm from the normal inspection and 17 mm from the parallel inspection, giving an average of about 19 mm as the estimated V2 length. This result is close to the visual estimation of about 22 mm in crack length. The results further show that the filtered imaging combined with the crack line extraction provides an effective and direct way to evaluate line SCC cracks even for that of smaller dimension. Note that the NDE inspected crack length is different from the finite element method (FEM) estimation (half length at 39 mm). This might be due to the fact that actual cracking situation is different from those simulated in the model or the entire length of V2 is beyond the detection resolution of the GUW NDE method. Further study as well as other NDE means to evaluate the crack lengths will be conducted in the future to understand the discrepancy.

5 Conclusions

A welded A285 carbon steel plate was fabricated with designed EDM starter cracks to approximate possible defect configurations in the weld region of high-level nuclear waste storage tanks. SCC was expected to occur when the test plate was exposed to a simulated waste tank chemistry condition. Theoretical prediction from the finite element analysis demonstrated that SCC could take place from the through-thickness starter cracks across the weld (designated as V1, V2, and V3 in Sec. 2.1). Visual examination of the test plate in the laboratory showed that the longest SCC occurred at V1 and the shortest at V2. Therefore, these two stress corrosion cracks were inspected for benchmarking the development of the present GUW NDE methodology.

The areas around the SCC V1 and V2 were inspected by GUW NDE using a PZT-SLDV system. The PZT wafer actuated the guided waves at a selected inspection frequency while the SLDV scanned the area of interest in the plate to obtain time–space wavefield data. Two inspection schemes were adopted in this study with different directions of incident wavefront with respect to the length direction of the SCC: (1) normal inspection with the incident wavefront normal to the length of the SCC and (2) parallel inspection with wavefront aligned to the SCC direction. Discernible waves–SCC interaction patterns have been observed in the regions where the crack as strong reflections from SCC for normal inspection and trapped waves with intensified wave energy along the length of SCC for parallel inspection, respectively. However, as seen in the energy images (Fig. 9), other than the wave interactions with the crack, the incoming waves from the PZT actuators toward the SCC are also present and may lead to misinterpretation of the detection if the details of the inspection setup are not fully understood. To achieve better quantification of the cracks, a filtering reconstruction imaging process was adopted in this study. The technique filtered out the interaction waves at the crack locations and then generated an image based on the energy intensity distribution in the plate, such that the SCC showed up as highlighted areas in the image of the plate. The energy intensity-based image was then further post-processed to create a "crack line image" with improved resolution and quality. The results from the filtering imaging method and the subsequent crack line extraction give an estimation of the V1 stress corrosion crack length at about 65 mm, which is close to that estimated by visual examination (about 70 mm). The methods were also applied to the shortest SCC (V2) on the plate. Due to much smaller crack dimension, very weak wave–crack interactions were observed and, subsequently, an image with limited quality was obtained (Fig. 13, left) from the filtering imaging method. However, with the crack line extraction post-processing, the V2 SCC was successfully identified and resulted in an estimation of half crack length at about 19 mm, compared with the visual estimation of 22 mm. Therefore, the GUW NDE has confirmed the presence of both V1 and V2 SCC and provides close estimation of their length. While most previous work was focused on idealized EDM cracks in thin metal plates, our work demonstrates the ability of GUW of detecting and estimating the length of barely visible SCC in a thick carbon steel plate with rugged surface. The filtering process combined with the line extract algorithm provides a quick and effective way for barely visible crack estimation. Currently, there is a discrepancy in the estimation of V2 SCC between the finite element prediction and the NDE measurement. Further study will be conducted in the future to understand and to resolve the inconsistency. At this stage, FEA is used mainly as an indicator to enable the adoption of NDE inspection. Additional SCC evaluation means to validate the GUW NDE inspection and estimation will be explored. Finally, focused research on GUW in the target material structures shall be conducted to gain a full understanding of wave propagation and interactions with SCC.

Acknowledgment

The authors are grateful for the financial support from the U.S. Department of Energy (DOE), Office of Nuclear Energy, under Grant Nos. DE-NE 0008959 and DE-NDE NE0008894.

Conflict of Interest

There are no conflicts of interest.

References

[1] Lam, P.-S., Cheng, C., Chao, Y. J., Sindelar, R. L., Stefek, T. M., and Elder, J. B., "Stress Corrosion Cracking of Carbon Steel Weldments," Proc. ASME 2005 Pressure Vessels and Piping Conference, Denver, CO, July 17–21, pp. 155–163.

[2] Wiersma, B., and Elder, J., 2008, "A Structural Impact Assessment of Flaws Detected During Ultrasonic Examination of Tank 15," Paper No. SRNS-STI-2008-0028, Savannah River National Laboratory.

[3] Kim, D., Udpa, L., and Udpa, S., 2004, "Remote Field Eddy Current Testing for Detection of Stress Corrosion Cracks in Gas Transmission Pipelines," Mater. Lett., **58**(15), pp. 2102–2104.

[4] Bosch, R.-W., 2005, "Electrochemical Impedance Spectroscopy for the Detection of Stress Corrosion Cracks in Aqueous Corrosion Systems at Ambient and High Temperature," Corros. Sci., **47**(1), pp. 125–143.

[5] Ramadan, S., Gaillet, L., Tessier, C., and Idrissi, H., 2008, "Detection of Stress Corrosion Cracking of High-Strength Steel Used in Prestressed Concrete Structures by Acoustic Emission Technique," Appl. Surf. Sci., **254**(8), pp. 2255–2261.

[6] Kovac, J., Alaux, C., Marrow, T. J., Govekar, E., and Legat, A., 2010, "Correlations of Electrochemical Noise, Acoustic Emission and Complementary Monitoring Techniques During Intergranular Stress-Corrosion Cracking of Austenitic Stainless Steel," Corros. Sci., **52**(6), pp. 2015–2025.

[7] Du, G., Li, J., Wang, W., Jiang, C., and Song, S., 2011, "Detection and Characterization of Stress-Corrosion Cracking on 304 Stainless Steel by Electrochemical Noise and Acoustic Emission Techniques," Corros. Sci., **53**(9), pp. 2918–2926.

[8] Zeitvogel, D. T., Matlack, K. H., Kim, J.-Y., Jacobs, L. J., Singh, P. M., and Qu, J., 2014, "Characterization of Stress Corrosion Cracking in Carbon Steel Using Nonlinear Rayleigh Surface Waves," NDT & E Int., **62**, pp. 144–152.
[9] Rose, J. L., 2014, *Ultrasonic Guided Waves in Solid Media*, Cambridge University Press, New York.
[10] Giurgiutiu, V., 2008, *Structural Health Monitoring: With Piezoelectric Wafer Active Sensors*, Elsevier, New York.
[11] Kim, S. B., and Sohn, H., 2007, "Instantaneous Reference-Free Crack Detection Based on Polarization Characteristics of Piezoelectric Materials," Smart Mater. Struct., **16**(6), pp. 2375–2387.
[12] Yu, L., and Giurgiutiu, V., 2008, "In Situ 2-D Piezoelectric Wafer Active Sensors Arrays for Guided Wave Damage Detection," Ultrasonics, **48**(2), pp. 117–134.
[13] Davies, J., and Cawley, P., 2009, "The Application of Synthetic Focusing for Imaging Crack-Like Defects in Pipelines Using Guided Waves," IEEE Trans. Ultrason. Ferroelectr. Freq. Control, **56**(4), pp. 759–771.
[14] Chen, X., Michaels, J. E., Lee, S. J., and Michaels, T. E., 2012, "Load-Differential Imaging for Detection and Localization of Fatigue Cracks Using Lamb Waves," NDT & E Int., **51**, pp. 142–149.
[15] Yu, L., and Tian, Z., 2013, "Lamb Wave Structural Health Monitoring Using a Hybrid PZT-Laser Vibrometer Approach," Struct. Health Monit., **12**(5–6), pp. 469–483.
[16] Masserey, B., and Fromme, P., 2017, "Analysis of High Frequency Guided Wave Scattering at a Fastener Hole With a View to Fatigue Crack Detection," Ultrasonics, **76**, pp. 78–86.
[17] Hernandez-Valle, F., Clough, A., and Edwards, R., 2014, "Stress Corrosion Cracking Detection Using Non-Contact Ultrasonic Techniques," Corros. Sci., **78**, pp. 335–342.
[18] Masserey, B., and Fromme, P., 2015, "In-Situ Monitoring of Fatigue Crack Growth Using High Frequency Guided Waves," NDT & E Int., **71**, pp. 1–7.
[19] Yu, L., Tian, Z., and Leckey, C. A., 2015, "Crack Imaging and Quantification in Aluminum Plates With Guided Wave Wavenumber Analysis Methods," Ultrasonics, **62**, pp. 203–212.
[20] Lu, M., Zhu, K., and Wang, Q., 2021, "Fatigue Crack Detection in Steel Plates Using Guided Waves and an Energy-Based Imaging Approach," Struct. Durability Health Monit., **15**(3), pp. 207–225.
[21] Qin, X., Zhang, S., Xu, C., Xie, J., Chen, G., and Song, G., 2020, "Detection of Surface Breaking Cracks Filled With Solid Impurities Using a Baseline-Free NEWS-TR Method," IEEE Access, **8**, pp. 56908–56920.
[22] Wang, J., Shen, Y., Rao, D., and Xu, W., 2021, "An Instantaneous-Baseline Multi-Indicial Nonlinear Ultrasonic Resonance Spectral Correlation Technique for Fatigue Crack Detection and Quantification," Nonlinear Dyn., **103**(1), pp. 677–698.
[23] Wang, J., Shen, Y., Rao, D., and Xu, W., 2021, "Physical-Virtual Time Reversing of Nonlinear Lamb Waves for Fatigue Crack Detection and Quantification," Mech. Syst. Signal Process., **160**, p. 107921.
[24] Zima, B., and Kędra, R., 2020, "Detection and Size Estimation of Crack in Plate Based on Guided Wave Propagation," Mech. Syst. Signal Process., **142**, p. 106788.
[25] Giurgiutiu, V., 2005, "Tuned Lamb Wave Excitation and Detection With Piezoelectric Wafer Active Sensors for Structural Health Monitoring," J. Intell. Mater. Syst. Struct., **16**(4), pp. 291–305.
[26] An, Y.-K., Kwon, Y., and Sohn, H., 2013, "Noncontact Laser Ultrasonic Crack Detection for Plates With Additional Structural Complexities," Struct. Health Monit., **12**(5–6), pp. 522–538.
[27] Lee, J.-R., Jang, J.-K., and Kong, C.-W., 2014, "Fully Noncontact Wave Propagation Imaging in an Immersed Metallic Plate With a Crack," Shock Vib., **2014**.
[28] Ostachowicz, W., Radzieński, M., and Kudela, P., 2014, "50th Anniversary Article: Comparison Studies of Full Wavefield Signal Processing for Crack Detection," Strain, **50**(4), pp. 275–291.
[29] Staszewski, W., Lee, B., and Traynor, R., 2007, "Fatigue Crack Detection in Metallic Structures With Lamb Waves and 3D Laser Vibrometry," Meas. Sci. Technol., **18**(3), pp. 727–739.
[30] Tse, W. T. P., and Masurkar, F., 2017, "A Novel and Fully Non-Contact Type of Laser System for Generating and Receiving Lamb Waves to Detect Cracks Occurred in I-Beams," Proceedings of the NDT in Canada 2017, Québec, Canada, June 6–8.
[31] Xiao, W., Yu, L., Joseph, R., and Giurgiutiu, V., 2020, "Fatigue-Crack Detection and Monitoring Through the Scattered-Wave Two-Dimensional Cross-Correlation Imaging Method Using Piezoelectric Transducers," Sensors, **20**(11), p. 3035.
[32] Norli, P., Vallée, E., Aanes, M., Spilde, A., Duerud, H., Prieur, F., Bjåstad, T., Standal, Ø, and Frijlink, M., "Ultrasonic Detection of Stress Corrosion Cracks in Gaseous Atmosphere Using Broadband Transducers," Proceedings of Meetings on Acoustics ICU, Bruges, Belgium, Sept. 3–6, Acoustical Society of America, p. 045037.
[33] Zapp, P. E., and Lam, P.-S., 2000, "Preliminary Evaluation of Tank 15 Vapor Space Cracking," Savannah River Site (US).
[34] Chao, Y. J., Qi, X., and Tang, W., 2003, "Heat Transfer in Friction Stir Welding —Experimental and Numerical Studies," ASME J. Manuf. Sci. Eng., **125**(1), pp. 138–145.
[35] Chao, Y.-J., and Qi, X., 1999, "Three-Dimensional Modeling of Gas Metal Arc Welding Process," Trans. North Am. Manuf. Res. Inst. SME, pp. 117–122.
[36] Chao, Y., Zhu, X., and Qi, X., 2000, "'WELDSIM—A WELDing SIMulation Code for the Determination of Transient and Residual Temperature, Stress, and Distortion," Adv. Comput. Eng. Sci., **2**, pp. 1207–1211.
[37] Hibbitt, Karlsson & Sorensen, Inc., 2001, *ABAQUS* Standard Version 6.2-1, ABAQUS, Pawtucket, RI.
[38] Leong, W., Staszewski, W., Lee, B., and Scarpa, F., 2005, "Structural Health Monitoring Using Scanning Laser Vibrometry: III. Lamb Waves for Fatigue Crack Detection," Smart Mater. Struct., **14**(6), pp. 1387–1395.
[39] Staszewski, W., Lee, B., Mallet, L., and Scarpa, F., 2004, "Structural Health Monitoring Using Scanning Laser Vibrometry: I. Lamb Wave Sensing," Smart Mater. Struct., **13**(2), pp. 251–260.
[40] Rogge, M. D., and Leckey, C. A., 2013, "Characterization of Impact Damage in Composite Laminates Using Guided Wavefield Imaging and Local Wavenumber Domain Analysis," Ultrasonics, **53**(7), pp. 1217–1226.
[41] Ma, Z., and Yu, L., 2021, "Lamb Wave Imaging With Actuator Network for Damage Quantification in Aluminum Plate Structures," J. Intell. Mater. Syst. Struct., **32**(2), pp. 182–195.
[42] Sohn, H., Dutta, D., Yang, J.-Y., Park, H.-J., DeSimio, M., Olson, S., and Swenson, E., 2011, "Delamination Detection in Composites Through Guided Wave Field Image Processing," Compos. Sci. Technol., **71**(9), pp. 1250–1256.
[43] Tian, Z., Yu, L., Leckey, C., and Seebo, J., 2015, "Guided Wave Imaging for Detection and Evaluation of Impact-Induced Delamination in Composites," Smart Mater. Struct., **24**(10), p. 105019.
[44] Michaels, J. E., 2017, "Ultrasonic Wavefield Imaging: Research Tool or Emerging NDE Method?," AIP Conference Proceedings, AIP Publishing LLC, Vol.1806, No. 1, p. 020001.
[45] Michaels, T. E., Michaels, J. E., and Ruzzene, M., 2011, "Frequency–Wavenumber Domain Analysis of Guided Wavefields," Ultrasonics, **51**(4), pp. 452–466.
[46] Ruzzene, M., 2007, "Frequency–Wavenumber Domain Filtering for Improved Damage Visualization," *Ultrasonic and Advanced Methods for Nondestructive Testing and Material Characterization*, C. H. Chen, ed., World Scientific, Singapore, pp. 591–611.
[47] Ma, Z., and Yu, L., 2019, "Lamb Wave Defect Detection and Evaluation Using a Fully Non-Contact Laser System," Proceedings of the Health Monitoring of Structural and Biological Systems XIII, Denver, CO, Mar. 3–7, International Society for Optics and Photonics, p. 1097221.